



Open Archive TOULOUSE Archive Ouverte (OATAO)

OATAO is an open access repository that collects the work of Toulouse researchers and makes it freely available over the web where possible.

This is an author-deposited version published in : <http://oatao.univ-toulouse.fr/>
Eprints ID : 9615

To link to this article : DOI:10.1080/00221686.2012.686457
URL : <http://dx.doi.org/10.1080/00221686.2012.686457>

To cite this version : Joly, Antoine and Violeau, Damien and Moulin, Frédéric and Astruc, Dominique and Kassiotis, Christophe. *Transport of isotropic particles in a partially obstructed channel flow*. (2012) Journal of Hydraulic Research, vol. 50 (n° 3). pp. 324-337. ISSN 0022-1686

Any correspondence concerning this service should be sent to the repository administrator: staff-oatao@listes-diff.inp-toulouse.fr

Transport of isotropic particles in a partially obstructed channel flow

ANTOINE JOLY, *Saint-Venant Laboratory for Hydraulics, Université Paris-Est, Joint Research Unit EDF/CETMEF/ENPC, 6 quai Watier, Chatou 78401, France.*

Email: antoine.joly@edf.fr

DAMIEN VIOLEAU (IAHR Member), *Saint-Venant Laboratory for Hydraulics, Université Paris-Est, Joint Research Unit EDF/CETMEF/ENPC, 6 quai Watier, Chatou 78401, France.*

Email: damien.violeau@edf.fr (author for correspondence)

FREDERIC MOULIN, *INPT, UPS, IMFT, Université de Toulouse, Allée Camille Soula, F-31400 Toulouse, France; CNRS, IMFT, F-31400 Toulouse, France.*

Email: frederic.moulin@imft.fr

DOMINIQUE ASTRUC (IAHR Member), *INPT, UPS, IMFT, Université de Toulouse, Allée Camille Soula, F-31400 Toulouse, France; CNRS, IMFT, F-31400 Toulouse, France.*

Email: dominique.astruc@imft.fr

CHRISTOPHE KASSIOTIS, *Saint-Venant Laboratory for Hydraulics, Université Paris-Est, Joint Research Unit EDF/CETMEF/ENPC, 6 quai Watier, Chatou 78401, France.*

Email: christophe.kassiotis@enpc.fr

ABSTRACT

The transport of particles in turbulent flows is a common problem in hydraulic engineering. In this paper, the focus is set on a numerical model used to simulate the transport of small bodies (debris, algae, etc.) along a coastline. In this problem, the particles are larger than the small turbulent eddies, but smaller than the large turbulent eddies, and sufficiently diluted within the flow so that each particle does not affect the flow or the motion of other particles. A mixed Eulerian–Lagrangian approach was chosen in order to model a large flow area with sufficient information for the turbulent diffusion. This model is validated through an experiment on particles released into a partially obstructed channel flow. The measurements are then compared with simulations using two Eulerian industrial codes, Telemac-2D and OpenFoam. Finally, an application to algae bloom transport in a harbour is presented.

Keywords: Lagrangian model; partially obstructed channel; particle diffusion; stochastic transport; video particle tracking

1 Introduction

For the sustainable management of industrial structures along the shoreline, it is a necessity to predict the motion of algae or debris transported along the shore, to prevent any loss of access to sea water. In the following, we will develop a model for the prediction of algae motion. Typically, models for the behaviour of algae along a coastline focus on the growth and the evolution of a population of algae (Donaghay and Osborn 1997, Salomonsen *et al.* 1999). However, when considering the problems that can affect the operation of industrial structures built on a coastline,

smaller time scales are involved (1 h–1 day as opposed to 1 day – a month). General observations have shown that algal blooms transported along the coast are very diluted (Joly 2011). This leads to the first hypothesis that to predict the motion of algae particles along the shoreline, the motion of each body (or particle) does not affect the flow in general, or the motion of another particle. This is useful as it allows a one way fluid–particle approach to be considered. Therefore, two models are used herein to predict the motion of algae particles along the shoreline. A first model will predict the large-scale effects of the flow, for example, tidal currents or non-uniform bathymetry and a second model will

predict the smaller scale effect of the particle motion. This is a standard approach when considering particle motion in a flow, for example, see, Issa *et al.* (2009), Monti and Leuzzi (2010), Frey *et al.* (1993) or Domgini *et al.* (1997).

The particles considered in this paper are large enough to only be affected by a certain range of turbulent eddies, but they are small enough that they do not hinder the fluid, differentiating the model presented here from typical solid particle transport such as sediment transport (Yeganeh-Bakhtiary *et al.* 2009, Bialik 2011). For the real applications of this model, the particles can be considered to be smaller than one-tenth of the large turbulent eddies in the flow and approximately 10 times larger than small turbulent eddies. This means that a particle does not modify the fluid velocities around it, but that the inertial properties of each particle cannot be ignored. Furthermore, each particle is distinct and, therefore, a Lagrangian model for the transport of particles will be used. Finally, to predict accurately the diffusion of an ensemble of particles, turbulence needs to be taken into account. The fluid–particle coupling allows the large-scale mean flow characteristics along the coast to be calculated efficiently with an Eulerian model. The Lagrangian particle transport model described in this paper will then input these mean flow characteristics into a stochastic model, which will give the turbulent fluid velocity fluctuations at the location of a particle. These will then be used in combination with the inertial properties of a particle, to predict the motion of an ensemble of particles.

In the literature, there exists different types of Lagrangian particle transport models that resemble the model presented in this paper. In addition to the models mentioned previously which focused on algae (Donaghay and Osborn 1997, Salomonsen *et al.* 1999) or sediment (Yeganeh-Bakhtiary *et al.* 2009, Bialik 2011) transport, there exists models such as the ones presented in Monti and Leuzzi (2010), Issa *et al.* (2009), Heemink (1990) or Stijnen *et al.* (2006) which predict the motion of particles in environmental flows by adding to the mean flow an estimation of the diffusion due to turbulence through the use of a diffusion constant. These models follow Brownian motion and none of the physical characteristics of the bodies are taken into account. Therefore, these models cannot be used for the problem at hand. Models predicting the transport of aerosols or bubbles, such as the models presented in Csanady (1963), Minier and Peirano (2001), Sawford and Guest (1991) or Yeo *et al.* (2010) consider the physical properties of the particles. However, these models are developed for small particles with a large density difference to the surrounding fluid. Furthermore, these models typically require more information on the flow than is generally available in hydraulic environmental flow modelling and, therefore, tend to only be applicable to a smaller scale of fluid models. These two facts make these models inapplicable to the algae problem. It is also possible to consider larger particles in the flow with direct numerical simulations, see, Uhlmann (2008), for example, but these models can only be used for a very small scale of simulation.

The model presented in this paper is compared with experimental results for isotropic particles released in a

partially obstructed channel. This configuration produces an inhomogeneous turbulent field, where the trajectories of the particles are recorded using a camera. Further simulations will be presented where particles are released in the flow covering a real bathymetry.

Therefore, this paper has three parts. First, the numerical model for the transport of solid particles in turbulent flows is presented. This is followed by the description experiments for particles released in a partially obstructed channel. Finally, the model is tested in a realistic bathymetry.

2 Particle transport model

The prediction of solid particle motion within a fluid requires the fluid velocities to be known at the location of each individual particles. These fluid velocities can then be used, along with the dynamic properties of the particle, to model its velocities.

2.1 The fluid velocity model

As mentioned in the introduction, a large-scale simulation of the mean fluid properties of the flow is run. This allows a large domain to be considered, and key physical processes (tides, waves or the effect of the bathymetry) can be modelled efficiently. However, this now requires another model to be applied to predict the local, smaller scale, turbulent fluid velocity fluctuations at the position of each particle.

The turbulence model applied here is the simplified Langevin model developed by Pope (1994, 2000). It is a simple Lagrangian model which is commonly used to model the dispersion of particles, see, Minier and Peirano (2001) or Joly *et al.* (2010). The first hypothesis of the stochastic model of turbulence is that the small turbulent eddies can be modelled using a white noise. The turbulence, which is generally non-homogenous, decaying and anisotropic, is then assumed to follow a linear return-to-isotropy model, making this stochastic model equivalent to Rotta’s model (Pope 1994). In the model, the assumption that the turbulence experiences a linear return to isotropy is used to model the kinematic viscosity and pressure fluctuations effects. Therefore, the fluid velocity variation along a fluid trajectory is given by (Pope 2000):

$$dU_i = -\frac{1}{\rho} \frac{\partial \bar{P}}{\partial x_i} dt + \left(\frac{1}{2} + \frac{3}{4} C_0 \right) \frac{\varepsilon}{k} (U_i - \bar{U}_i) dt + \sqrt{C_0 \varepsilon} dW_i \quad (1)$$

where U_i represents the i th component of the fluid velocity, P is the fluid pressure, k is the TKE, ε is the TKE dissipation rate, C_0 is a diffusion constant equal to 2.1, W_i is a Wiener process, for which $dW_i dW_j = dt \delta_{ij}$. All variables are given for a particle at time t and particle position X_i . Furthermore, the overline used, e.g. “ $\bar{\quad}$ ”, represents Reynolds-averaged values.

Now that the fluid velocities at the location of a particle can be solved, we look at the response of a solid particle to those fluid velocities.

2.2 The solid particle dynamics

Most papers that consider the motion of a solid body in a flow focus on spherical particles that are small compared with the smaller scales of turbulence (limited to a maximum particle size equal to 0.4 of the small turbulent eddies characteristic length), see, for example, Maxey and Riley (1994), Minier and Peirano (2001) or van Hinsberg *et al.* (2011). However, in this paper, we are interested in larger particles. Each force considered will be introduced separately.

The first force which applies to a solid particle is the drag force, which represents the resistance of the body to the flow through friction or pressure difference along the body. This gives the motion for a solid particle as (Falkovich 2011):

$$m \frac{dV_i}{dt} = \frac{1}{2} \rho_f S C_D(\mathbf{R}) |\mathbf{U} - \mathbf{V}| (U_i - V_i) \quad (2)$$

where \mathbf{U} and \mathbf{V} are the fluid and particle velocity vectors, respectively, V_i represents the i th component of the particle velocity, m represents the mass of the particle, given by the particle density ρ_s multiplied by the volume of the particle Ω . ρ_f is the fluid density, S is the cross-sectional area of the particle and C_D is the drag coefficient. The latter is given as function of the particle Reynolds number \mathbf{R} :

$$\mathbf{R} = \frac{|\mathbf{U} - \mathbf{V}| D}{\nu} \quad (3)$$

with ν being the fluid molecular kinematic viscosity and D the characteristic size of the particle.

The second term considered here is the force necessary to overcome the inertia of the particle, as well as a portion of the fluid surrounding the particle (this second part is known as the added mass of the particle). Depending on the size and shape of the particles, this force can sometimes be neglected, but a formulation of this force is added to the model to allow future modifications to non-spherical particles (see, Gaylord *et al.* 1994 for the differences between spheres and algae). For this force to be accurate, it is assumed that the fluctuations of the fluid along the length scale of a particle are negligible, and that the fluid is at rest infinitely away from the particle (Landau and Lifchitz 1987). This then gives the following equation of motion for the particle:

$$m \frac{dV_i}{dt} = \rho_f \Omega \frac{dU_i}{dt} - M_{ij} \frac{d}{dt} (V_i - U_i) + \frac{1}{2} \rho_f S C_D(\mathbf{R}) |\mathbf{U} - \mathbf{V}| (U_i - V_i) \quad (4)$$

where M_{ij} is the added mass tensor.

An additional force that is often neglected due to its complexity is the Basset history force, which implies that the motion of a body depends on the previous evolution of the solid body and fluid velocities. The form of the force presented here and added

to the previous equation of motion (Eq. 4) is the one described in Corrsin and Lumley (1956):

$$m \frac{dV_i}{dt} = \rho_f \Omega \frac{dU_i}{dt} - M_{ij} \frac{d}{dt} (V_i - U_i) + \frac{1}{2} \rho_f S C_D(\mathbf{R}) |\mathbf{U} - \mathbf{V}| (U_i - V_i) + 6D^2 \rho_f \sqrt{\pi \nu} \int_{-\infty}^t \frac{1}{\sqrt{t-s}} \frac{d}{ds} (U_i - V_i) ds \quad (5)$$

This equation is only valid for small particles, as it assumes that the disturbance flow is at a low Reynolds number. Physically, this would not be true in our case. Extensions to the Basset history force exist, for example, see the model proposed in Maxey and Riley (1994) which includes the Faxen correction terms. To apply these corrections, the large-scale Eulerian model, which is necessary to provide the mean flow characteristics, would be required to provide the spatial derivatives of the mean fluid velocities. For large-scale hydraulic environmental models, these values are not easily known and, therefore, a simple formulation of the Basset history force has been chosen in this particle transport model.

Other forces can be introduced, but in our case they are ignored. Buoyancy effects will be neglected as the simulations later on are done solely for planar two-dimensional flows. However, these forces are very important in three-dimensional flows. In addition, the lift force has been ignored, since the particles transported by the flow are assumed irrotational. This assumption is done because taking into account the fluid velocity differences around a particle would require a finer resolution of the flow. Furthermore, this is consistent with the hypothesis that the velocity fluctuations are negligible along a length scale of the order of the characteristic size of the particle. To correctly take into account fluid velocity fluctuations around a body, a direct numerical simulation would be required, see, Uhlmann (2008), and the model would lose its industrial practicality.

All of the inertial properties of the particle presented in Eqs. (2)–(5) will create a response time of the particle to the fluid velocities, which will filter out the small scales of turbulence. Finally, as a starting point the particles are modelled as spheres for which the drag coefficient and the added mass tensor are given by Almedeij (2008) and Falkovich (2011), respectively:

$$C_D = \left[\frac{1}{(\varphi_1 + \varphi_2)^{-1} + (\varphi_3)^{-1}} + \varphi_4 \right]^{1/10} \quad (6a)$$

$$\varphi_1 = (24\mathbf{R}^{-1})^{10} + (21\mathbf{R}^{-0.67})^{10} + (4\mathbf{R}^{-0.33})^{10} + (0.4)^{10} \quad (6b)$$

$$\varphi_2 = \frac{1}{(0.148\mathbf{R}^{0.11})^{-10} + (0.5)^{-10}} \quad (6c)$$

$$\varphi_3 = (1.57 \times 10^8 \mathbf{R}^{-1.625})^{10} \quad (6d)$$

$$\varphi_4 = \frac{1}{(6 \times 10^{-17} \mathbf{R}^{2.63})^{-10} + (0.2)^{-10}} \quad (6e)$$

$$M_{ij} = \frac{1}{2} \rho \Omega \delta_{ij} \quad (7)$$

This final simplification is done by assuming that in an algae bloom, particles will fold over each other and change orientation. Therefore, in a general sense, they can be considered isotropic. However, for real-life applications, drag coefficient and added mass tensor should be calculated specifically for an alga, see, Gaylord *et al.* (1994).

2.3 Particle trajectories

From the previous two subsections, a three-step transport model has been developed:

$$dU_i = -\frac{1}{\rho} \frac{\partial \bar{P}}{\partial x_i} dt + \left(\frac{1}{2} + \frac{3}{4} C_0 \right) \frac{\varepsilon}{k} (U_i - \bar{U}_i) dt + \sqrt{C_0 \varepsilon} dW_i \quad (8a)$$

$$dV_i = \frac{F_{\text{applied}}}{m} dt \quad (8b)$$

$$dX_i = V_i dt \quad (8c)$$

for which the applied forces F_{applied} depend on the degree of information required, as defined by Eqs. (2), (4) or (5).

To solve numerically, the system of equations (8a)–(8c) can be tedious, and it is recommended to use an exact integrator method as described in Joly *et al.* (2010) or Joly (2011), while the Basset history force can be calculated using the method proposed by van Hinsberg *et al.* (2011). Furthermore, mean flow quantities are interpolated linearly to the location of the particle from the nodal values of the mesh solved by the Eulerian models. This is done classically in finite element methods (Hervouet 2007).

The model has been tested for spherical particles released in stationary quasi-isotropic grid turbulence. In Fig. 1, the probability density functions for the horizontal and vertical particle velocities are shown. It shows that the complete model, with the Basset history force, gives a good estimation of the solid

particle velocities. The physical characteristics for this experiment are $D/\lambda_l = 0.106$, $\rho_s/\rho_f = 1.12$, $S_{\text{set}} = 1.52$, $N_r = 354$, $R_{\text{set}} = 620$, where λ_l is the characteristic size of the large turbulent eddies, ρ_s/ρ_f is the density ratio, S_{set} is the ratio between the relaxation time of the particles and a characteristic turbulent time, N_r is the number of recordings and R_{set} is a particle Reynolds number calculated using the settling velocity. More details on the experimental set-up necessary for Fig. 1 as well as an explanation of the discrepancies between the numerical simulations and the experimental results can be found in Joly (personal communication).

3 Particles released in a partially obstructed channel flow

To validate the behaviour of the model presented in this paper in the case of a space-varying flow, and the coupling between the large-scale Eulerian flow model and a smaller scale stochastic Lagrangian particle transport model, a set of experiments has been undertaken.

3.1 Experimental set-up

The partially obstructed open flat-bed channel flow is a well-documented configuration, see, Ettema and Muste (2002), Tang *et al.* (2006) or Uijtewaal (2005). This flow has the advantage of presenting inhomogeneous turbulence. The experimental set-up is described in Figs. 2 and 3.

For the validation experiment, a flow rate of 0.5 m/s was imposed in a 2-m-wide channel which was obstructed by a dike 0.5 m long and 0.1 m thick. The water depth was imposed to 0.3 m before the flow arrived at the dike. Ettema and Muste (2002) have conducted several partially obstructed flat-bed open-channel flow experiments and they have observed that, generally, the recirculation zone occurring after the dike is of the order of

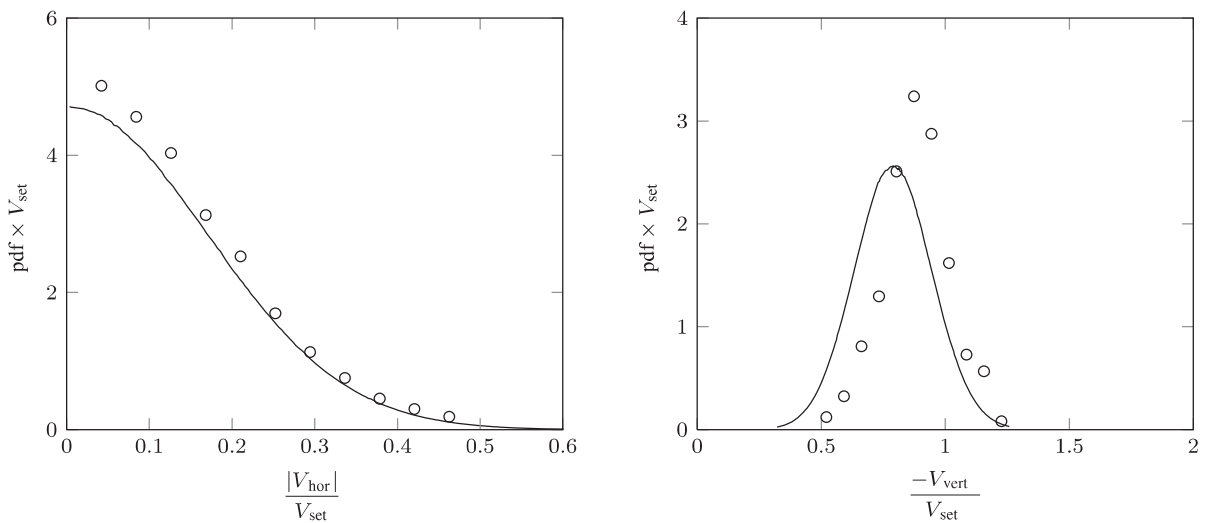


Figure 1 Probability density functions for horizontal and vertical settling particles in stationary quasi-isotropic grid turbulence, see, Joly (personal communication). “○” shows the experimental data and “—” shows the results from simulations considering all of the force components (Eq. 5). The velocities are non-dimensionalized using the settling velocities in the absence of turbulence V_{set}

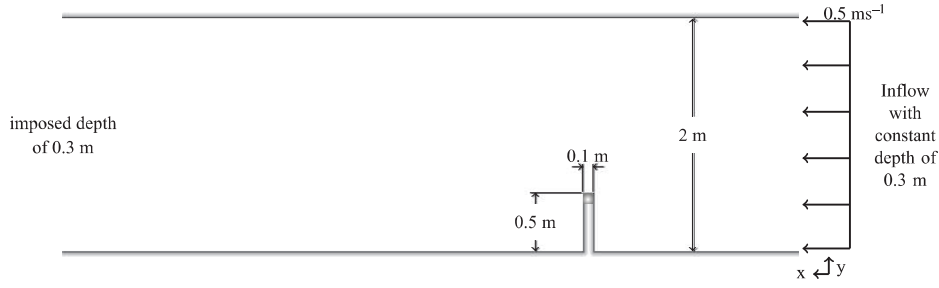
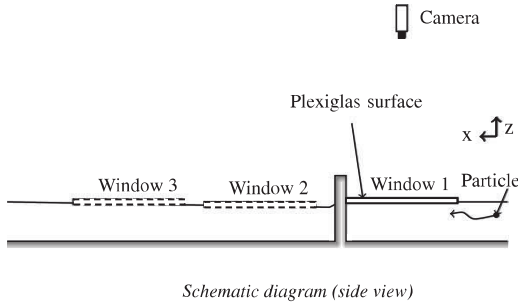


Figure 2 Experimental set-up for a partially obstructed flat-bed open-channel flow (top view)

(a)

(b)



Schematic diagram (side view)

Photograph

Figure 3 Experimental set-up (side view) and particle trajectories recording system

10–12 times the length of the dike. This zone is of particular interest, as it should trap particles released in the flow.

The water velocities were recorded with the three-dimensional acoustic doppler velocimeter (ADV). The equipment used is a Sontek head which detects the impurities in the fluid. The measurements were done with an acoustic frequency of 16 MHz, a sample volume equal to 0.1 cm^3 , a velocity measurement rate of 50 Hz and a velocity resolution of 0.01 cm/s . The record length for all the quantities measured was 120 s and the fluid velocities were recorded with an error of approximately 1%. The ADV head was placed using a grid that was 50 cm along the x -axis ranging from -2 to 5 m , and with extra measurements done at ± 0.1 and $\pm 0.3 \text{ m}$. Along the y -axis, measurements were conducted with a 20 cm spacing ranging from 0.27 to 1.67 m . Each measurement was done at three depths, 10, 15 and 20 cm , wherever possible. The ADV measurements were also performed at four depths, 5, 10, 15 and 20 cm , in the center of the channel and before the flow was affected by the dike. These points were chosen so that the measured fluid velocities could be compared with the numerical results.

However, care should be taken when measuring the turbulent velocities with an ADV. The recording rate needs to be high enough to observe all the turbulent structures. Furthermore, the number of samples needs to be large enough to reduce the error (Chanson 2008). In this experiment, velocity data were recorded at a rate of 50 Hz for 2 min. Six thousand samples were recorded, which should be sufficient as the characteristic time for the small turbulent eddies can be estimated $\tau_s = 0.02 \text{ s}$ and for the large turbulent eddies $\tau_l = 7 \text{ s}$.

A particle injector was designed to release a constant flow of spheres of 6 mm in diameter and 2200 kg/m^3 . These particles can

be assumed to enter the flow at rest and they can be characterized using the following non-dimensional parameters. The first one is the Stokes number which is a ratio between the particle relaxation time and the characteristic time of the small turbulent eddies:

$$S = \frac{\tau_p}{\tau_s} \quad (9a)$$

$$\tau_p = \frac{2\rho_s + \rho_f t)D^2}{36\nu\rho_f} \quad (9b)$$

$$\tau_s = \left(\frac{\nu}{\varepsilon}\right)^{1/2} \quad (9c)$$

In this case, the Stokes number is around 170. The second one is the density ratio between the solid particles and the fluid which is $\rho_s/\rho_f = 2.2$. Third, the particle Reynolds number that is given by Eq. 3.

When the particles enter the flow, they have a Reynolds number of about 3000. The final non-dimensional number which can be helpful is the gravity parameter, which is defined by

$$G_p = \frac{V_{\text{set}}}{U_{\text{rms}}} \quad (10)$$

where V_{set} is the settling velocity of the particles and U_{rms} is the root mean square fluid velocity. For this flow scenario, the gravity parameter is around 8.

Particles were released so that when entering the measurement window they had not settled fully. The trajectories were obtained with a camera recording 14 images per second. It should be noted that a flat Plexiglas surface had to be placed just on the surface of the flow to provide undisturbed images. The results are, therefore, only two-dimensional. Parallax was also tested, and it was

found to be negligible for this camera set-up. Due to the difficulty in obtaining *in situ* measurements for real applications, the experimental results will focus on the ability of the model to predict particles caught in the recirculation zone, so that the code can be used as a decision tool for further real applications involving similar phenomena. For more robust validation of the code, please refer to Joly *et al.* (2011).

3.2 Mean flow characteristics

The first results shown present the ability of two different Eulerian flow models to predict the recirculation zone. A simulation was done using Telemac-2D, which solves the shallow-water equations with a depth-averaged $k-\epsilon$ closure using a finite elements method (Hervouet 2007). This code is useful for large coastal flows, as it can deal with tidal flats. It was designed for industrial needs. Another simulation was done using OpenFoam, which solves the two-dimensional Navier–Stokes equations with a $k-\epsilon$

closure using a finite volumes method (Open CFD 2011). For both codes, the constants of the $k-\epsilon$ model are set to $C_{\epsilon 1} = 1.44$, $C_{\epsilon 2} = 1.92$, $\sigma_k = 1.0$ and $\sigma_\epsilon = 1.3$, such as defined in Launder and Sharma (1974).

In Figs. 4–6, the experimental and simulated fluid velocities in the direction of the flow, the TKE (k) and its dissipation rate (ϵ) are compared for a flow with a Reynold number equal to 10^6 . These fluid characteristics are plotted for different cross-sections of the flow. At the location of the cross-sections, the values of the fluid characteristic magnitude are shown just above the x -axis.

It should be noted that the meshes used in the numerical simulations have been refined to reduce the numerical errors. The final mesh used had a characteristic element size of 0.01 m around the dike, 0.1 m along the inflow boundary and the outflow boundary. A more refined mesh has been tested, but it did not improve the results. The total modelled domain ranged from $x = -5$ to 10 m and $y = 0$ to 2 m. This created a mesh consisting of 73,000 elements and 37,000 nodes. CFL conditions were imposed on

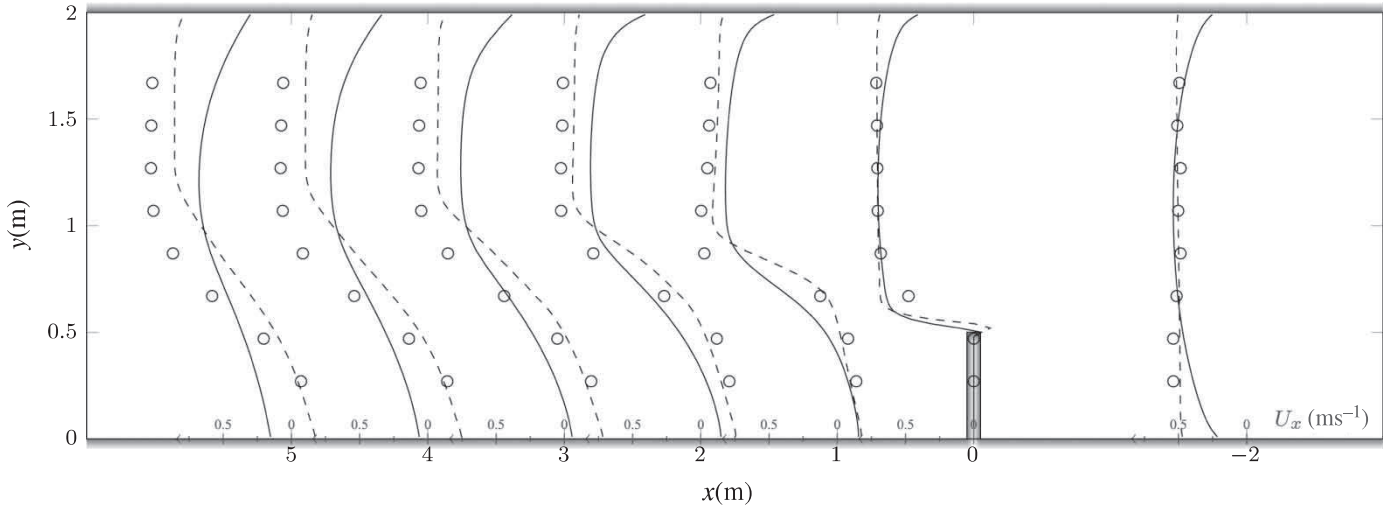


Figure 4 Profiles of the horizontal velocity plotted at different locations along the channel. The small axis mark on top of the x -axis represents the values of velocity magnitude. “○” are experimental results, “—” are results found using Telemac-2D and “- - -” are results found using OpenFoam

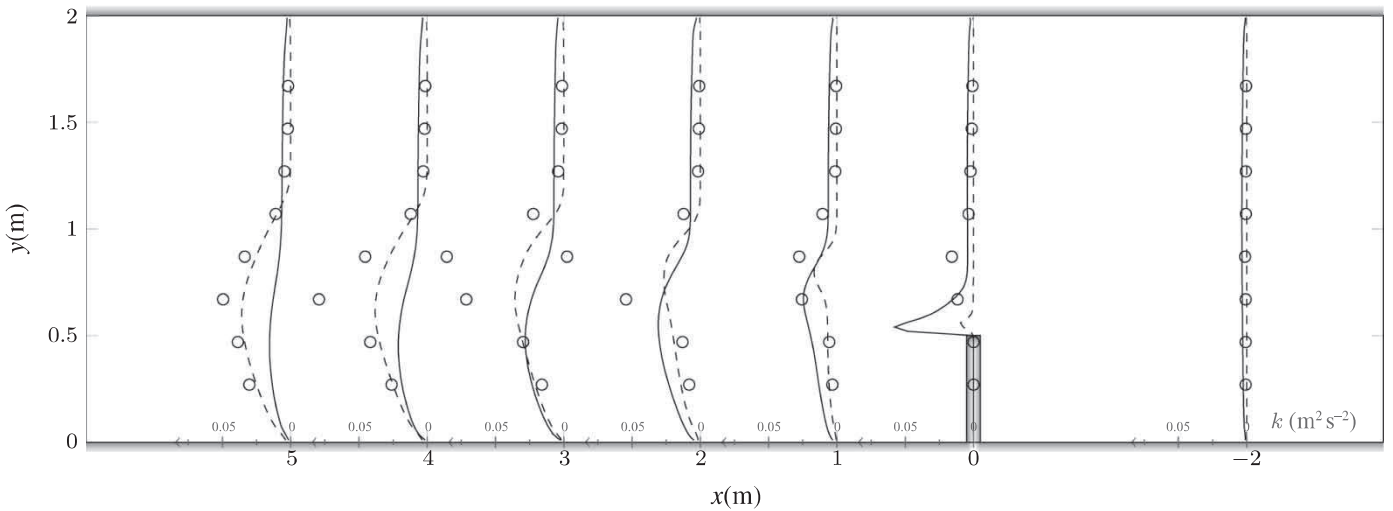


Figure 5 Profiles of the TKE plotted at different locations along the channel. The small axis mark on top of the x -axis represents the values of TKE. “○” are experimental results, “—” are results found using Telemac-2D and “- - -” are results found using OpenFoam

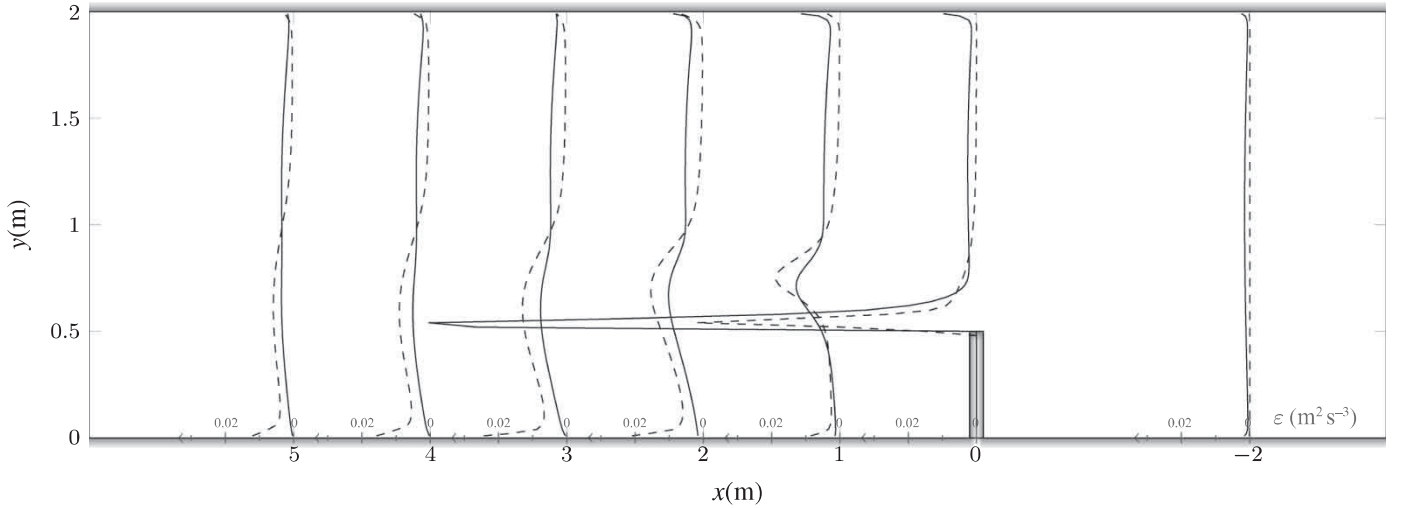


Figure 6 Profiles of the TKE dissipation rate plotted at different locations along the channel. The small axis mark on top of the x-axis represents the values of the energy dissipation. “—” are results found using Telemac-2D and “- - -” are results found using OpenFoam

each simulation done with the different meshes, and for the final chosen mesh, the numerical time step used was 0.01 s. Furthermore, a constant inflow with a flow rate of $0.3 \text{ m}^3 \text{ s}^{-1}$ has been imposed on the inflow section and a constant height of 0.3 m has been imposed for the outflow. Using these conditions, Telemac-2D and OpenFoam imposed different initial velocity profiles, which are plotted in Fig. 4 at $x = -2 \text{ m}$.

In Fig. 4, both profiles obtained by numerical simulations seem to be in accordance with the experiments. Nonetheless, the numerical models seem to be too diffusive, and they underestimate the size of the recirculation region. Furthermore, OpenFoam seems to model more accurately the velocities along the edge of the channel.

Figure 5 shows that both numerical models have more difficulties calculating the kinetic energy at the edge of the recirculation zone. Telemac-2D seems to estimate the TKE directly after the dike more accurately, but further downstream OpenFoam gives better values. The numerical values for the dissipation rate were also plotted in Fig. 6, but no experimental data were available. Telemac-2D seems to find much more dissipation directly after the dike. The sizeable difference between the simulations and the experiment is due to the fact that the $k-\varepsilon$ closure turbulence model is not able to predict the turbulent regime. Therefore, other turbulence models were tested within OpenFoam (Telemac-2D is not designed to use more complete turbulence models). The simulations done with a $k-\omega$ model only improved the results slightly. The simulations done using R_{ij} models were able to predict correctly the recirculation zone, but they required an initial state of the flow to be calculated using a $k-\varepsilon$ model. A further proof of the inability of the $k-\varepsilon$ closure turbulence model to predict the turbulent regime can be seen by the difference between the values simulated using Telemac-2D and OpenFoam in Figs. 5 and 6.

In conclusion, the $k-\varepsilon$ model will nonetheless be used within Telemac-2D and OpenFoam to simulate the average flow

characteristics necessary to simulate the transport of solid particles, as it is the most complete turbulence model present in both codes. However, the authors are aware of the limitations of the $k-\varepsilon$ turbulence model in the current flow configurations. The numerical results found from both industrial codes will be used by the stochastic turbulent fluid velocity model (Eq. 8a). The results from this model are then used to calculate the particle trajectories with Eqs. (8b) and (8c). The particle trajectories will be compared with experimental results.

3.3 Particle tracking

A camera was placed above the flow to record particles entering the measurement window, see Fig. 3. The horizontal coordinate system was chosen as in Fig. 2. Particles were released until the trajectories of over 100 particles were recorded from each initial position. It should be noted that most trajectories in the wake of the dike were incomplete due to the vortices generated. When this was the case, the particles were hidden to the camera, and when the particles re-appeared they were considered as new particles by the image-processing algorithm.

From each recorded image, it is possible to obtain the position of a particle, and a time series of such images gives the trajectories of each particle, see, Joly (2011) for a description of the method used. Two typical particle trajectories recorded by the camera are plotted in Fig. 7.

To analyse the trajectories of the particles, the windows of measurements are divided into four quadrants. From the recorded particle trajectories, we can observe the proportion of particles released into the flow entering each quadrant of the measurement window, as well as the mean time of residence inside this quadrant. The same thing was done for the artificial particles in the simulations. These results can be represented in such a way that for each quadrant the value of interest is plotted along a line going from the innermost corner to the outermost corner of this

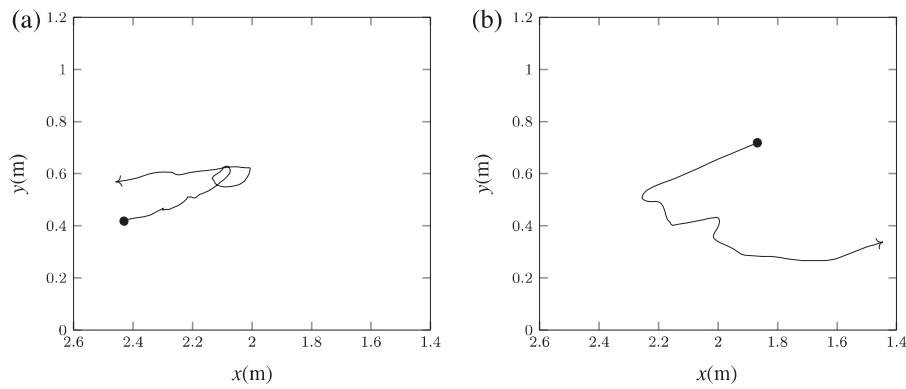


Figure 7 Typical particle trajectories

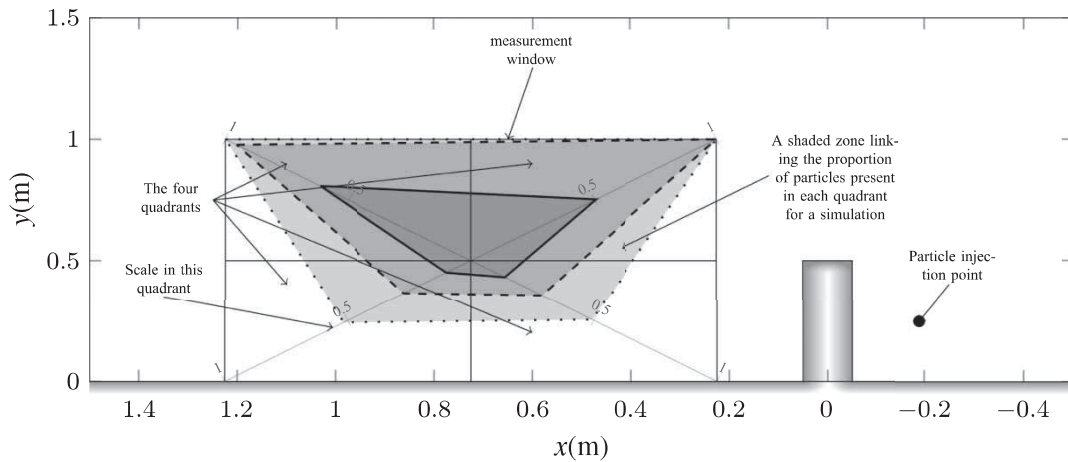





Figure 8 An annotated example to explain how the proportion of particles entering each quadrant of a measurement window are presented. “” shows the experimental results, “” shows the results using Telemac-2D and “” shows the results using OpenFoam

quadrant. The length scales for these values are chosen in such a way that the maximum value is placed on the outermost corner. The points plotted for each quadrant are then linked together to form an area. An annotated example is found in Fig. 8.

Experiments are compared with simulations where the flow is computed with two Eulerian models (Telemac-2D and OpenFoam), and the solid particles are simulated with a Lagrangian model, as defined by Eqs. (5) and (8a)–(8c). The proportion of particles entering a quadrant, which is defined as the number of particles entering a quadrant divided by the total number of particles present from the experimental or numerical results, is shown in Fig. 9. Figure 10 shows the mean residence time of particles, which is the average time a particle is present within a quadrant.

Figures 9 and 10 show that there is an acceptable correlation between numerical and experimental results in the number of particles entering each quadrant. The two Eulerian models prove fairly effective in their ability to predict the entrapment of particles. However, Fig. 9 indicates that particle trajectories calculated using OpenFoam seem to experience greater dispersion. Figure 10 shows that with Telemac-2D the residence time

of particles is overestimated in the quadrants close to a solid boundary. This is due to the fact that Telemac-2D overestimated the mean flow velocity close to the boundaries.

For the windows of measurement placed downstream of the dikes, the actual total number of particles present in each quadrant is much lower than the number of particles recorded in the experiment. This is because the recorded images were severely affected by the generation of vortices downstream of the dike, and the position of a particle would be lost for a few images. Furthermore, particles leaving the measurement window, and entering again will also be accounted for more than once. This means that one particle can be accounted for multiple times, meaning that the experimental results overestimate the total number of particles recorded while leaving all other parameters (such as the number of particles entering a quadrant) unaffected.

This explains why in Figs. 9 and 10 the areas of the experimental quadrilaterals downstream of the dike are smaller than for the numerical simulations. To counteract this experimental limit, the shape of the area plotted in Figs. 9 and 10 should be observed. The shapes of the quadrilaterals shown in Figs. 9 and

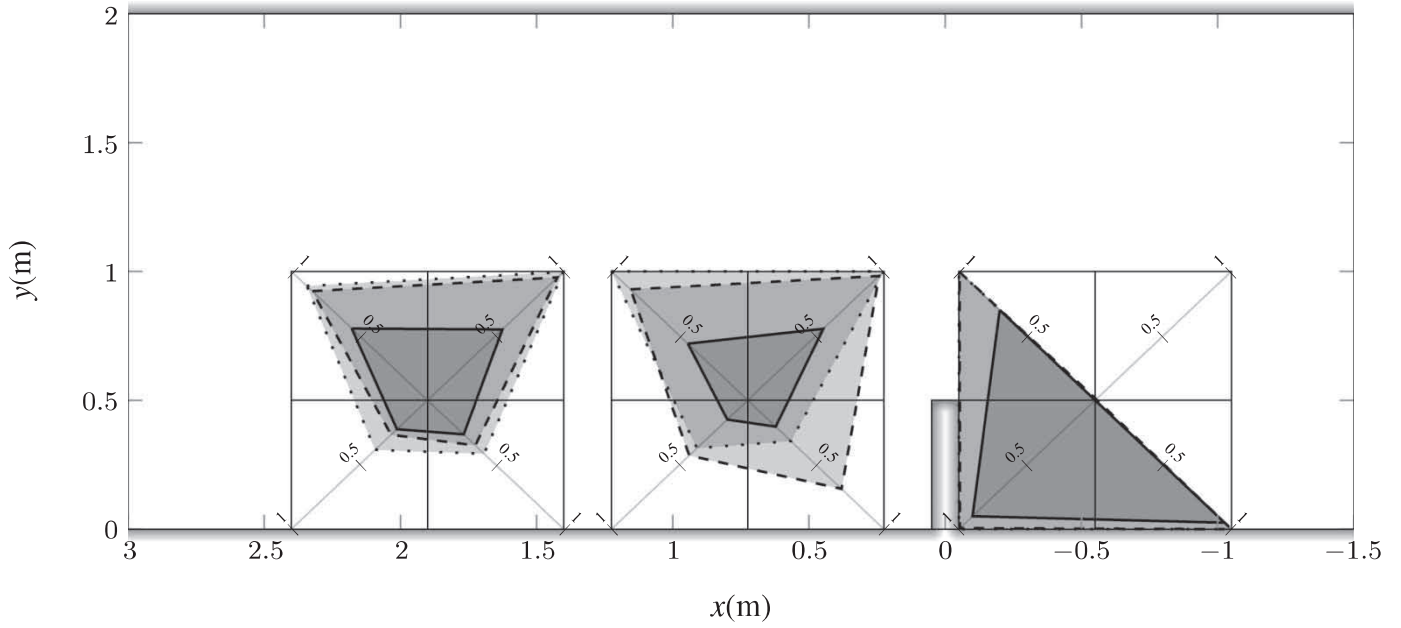


Figure 9 Partially obstructed channel: proportion of released particles entering a quadrant of the measurement window. “—” shows the experimental results, “- - -” shows the results using Telemac-2D and “...” shows the results using OpenFoam. The results shown in the measurement window 1 were released at point $(-1.3, 0.19)$ m and those shown in windows 2 and 3 were released at point $(0.175, 0.45)$ m

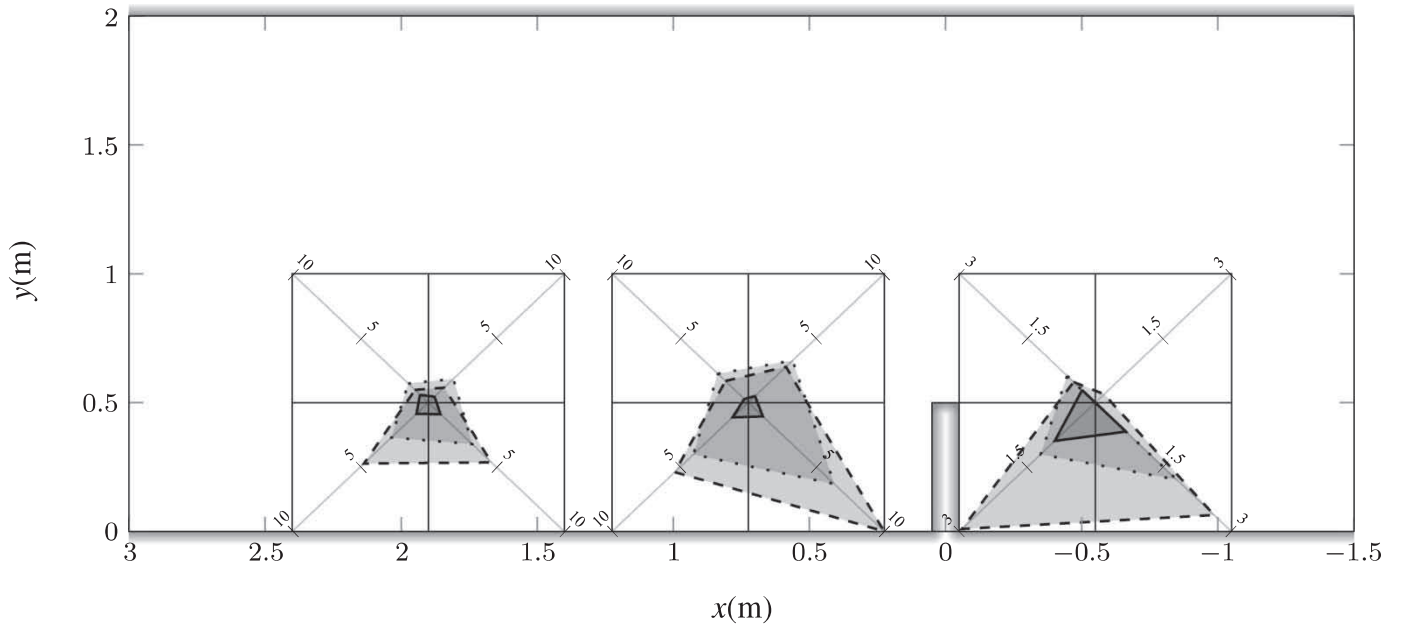


Figure 10 Partially obstructed channel: mean particles residence time inside a quadrant of the measurement window. The time is given in seconds. “—” shows the experimental results, “- - -” shows the results using Telemac-2D and “...” shows the results using OpenFoam. The results shown in the measurement window 1 were released at point $(-1.3, 0.19)$ m and those shown in windows 2 and 3 were released at point $(0.175, 0.45)$ m

10 can be analysed by looking at the ratios between the values of N_{prop} and t_{res} in the two top quadrants and the two bottom quadrants. These ratios, as shown in Table 1, show that the shape of the overall shaded areas of Figs. 9 and 10 is generally similar in the experimental and the numerical results.

There are a few discrepancies in Table 1. In window 1, the residence time (t_{res}) ratio between the top right quadrant and the top left quadrant seems greatly overestimated in the simulations

using Telemac-2D. This is because, due to the stochastic nature of the model, one particle in the simulation entered briefly the top right quadrant, which was not the case for the other recordings. Other discrepancies can be found, but these are greatest for the ratios of the bottom two quadrants of the second measurement window. These are most likely a result of the inability of both Eulerian codes to simulate the flow regime in the corner formed by the dike and the channel wall.

Table 1 Ratios of the proportion (N_{prop}) and the mean time of residence (t_{res}) of particles present in the top and bottom half of the measurement window

		Top right over top left		Bottom right over bottom left	
		N_{prop}	t_{res} (s)	N_{prop}	t_{res} (s)
Window 1; release = $(-1.3, 0.19)$	Experiment	0.000	0.000	1.060	0.758
	Telemac-2D	0.008	0.405	1.010	0.890
	OpenFoam	0.000	0.000	1.000	1.490
Window 2; release = $(0.175, 0.45)$	Experiment	1.260	1.770	1.370	0.934
	Telemac-2D	1.120	1.650	1.610	1.850
	OpenFoam	1.000	1.460	0.852	1.570
Window 3; release = $(0.175, 0.45)$	Experiment	0.988	0.748	1.180	1.040
	Telemac-2D	1.130	1.180	1.310	0.982
	OpenFoam	1.120	1.240	1.080	1.180
Window 2; release = $(0.98, 0.55)$	Experiment	0.821	1.070	1.390	0.444
	Telemac-2D	1.050	1.160	1.070	1.730
	OpenFoam	1.000	1.050	0.954	1.650

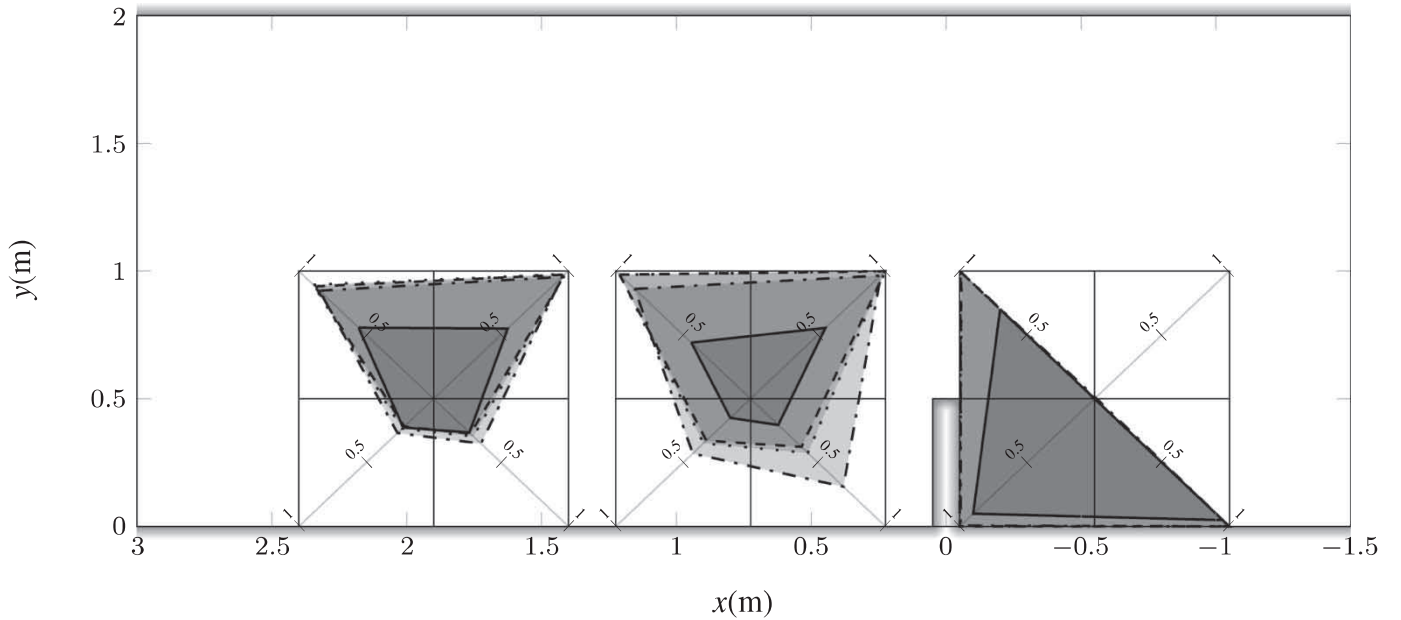


Figure 11 Partially obstructed channel: proportion of released particles entering a quadrant of the measurement window. “ \square ” shows the experimental results, “ \square ” shows the results from simulations considering only the drag forces (Eq. 2), “ \square ” shows the results from simulations considering the drag and momentum forces (Eq. 4) and “ \square ” shows the results from simulations considering all of the force components (Eq. 5). The results shown in the measurement window 1 were released at point $(-1.3, 0.19)$ m and those shown in windows 2 and 3 were released at point $(0.175, 0.45)$ m

Finally, because in Figs. 9 and 10 and in Table 1 Telemac-2D seems to be in better accordance with experimental results, when focusing on the shape of the shaded areas plotted in the windows of measurement, the effects of the force components of the solid particle dynamics will be tested using Telemac-2D, even if OpenFoam predicted the fluid velocities more accurately along the edge of the canal.

The effects of the different force components can be found in Figs. 11 and 12. For these figures, one should again look at the shape of the quadrilaterals, rather than the covered area. These figures show that the results found using different models are

very similar. This is because the particles chosen in these simulations are small, and the amount of information extracted from those simulations is very coarse. The plots of the model using all the force components (Eq. 5) show slightly better results, but it is hardly visible. However, Joly et al. (2011) showed that the particle velocities are better predicted with a more complete particle transport model. This makes the model better suited for real flows, and the prediction of transport over large areas, where minute early differences can become more apparent. Furthermore, having more information present in the model can make it adaptable to real inertial particle.

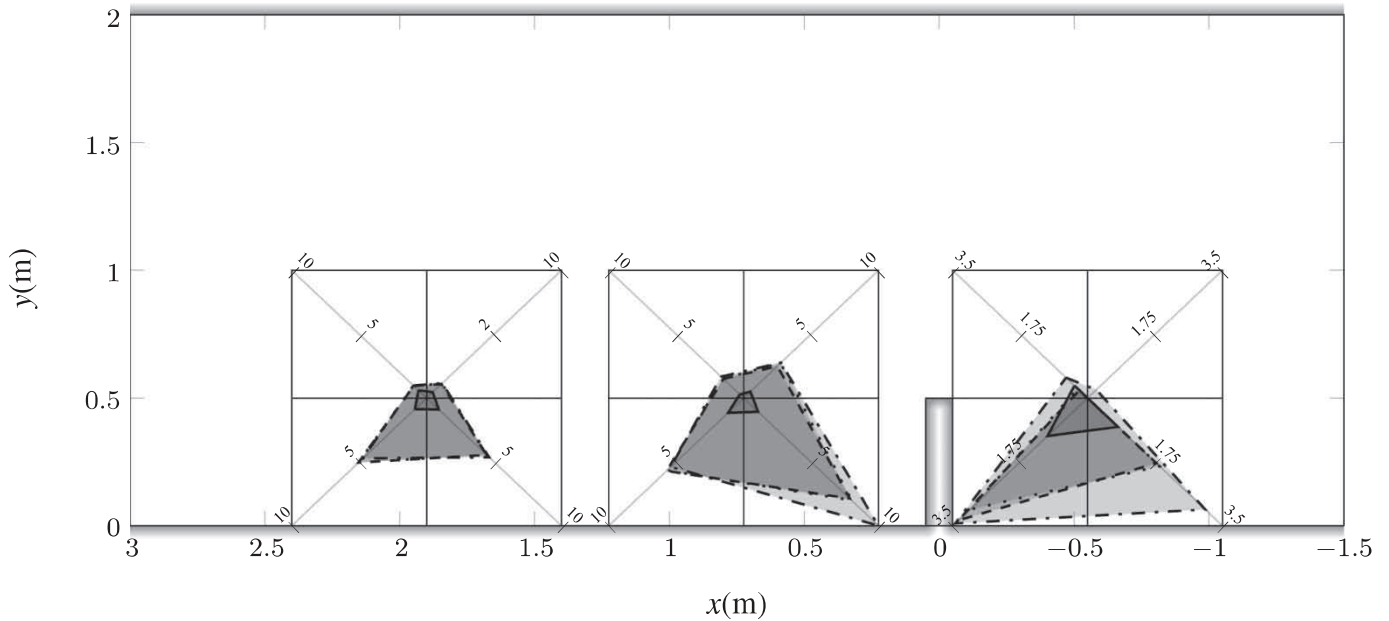


Figure 12 Partially obstructed channel: mean particles residence time inside a quadrant of the measurement window. “—” shows the experimental results, “- - -” shows the results from simulations considering only the drag forces (Eq. 2), “· · ·” shows the results from simulations considering the drag and momentum forces (Eq. 4) and “- · - ·” shows the results from simulations considering all of the force components (Eq. 5). The results shown in the measurement window 1 were released at point $(-1.3, 0.19)$ m and those shown in windows 2 and 3 were released at point $(0.175, 0.45)$ m

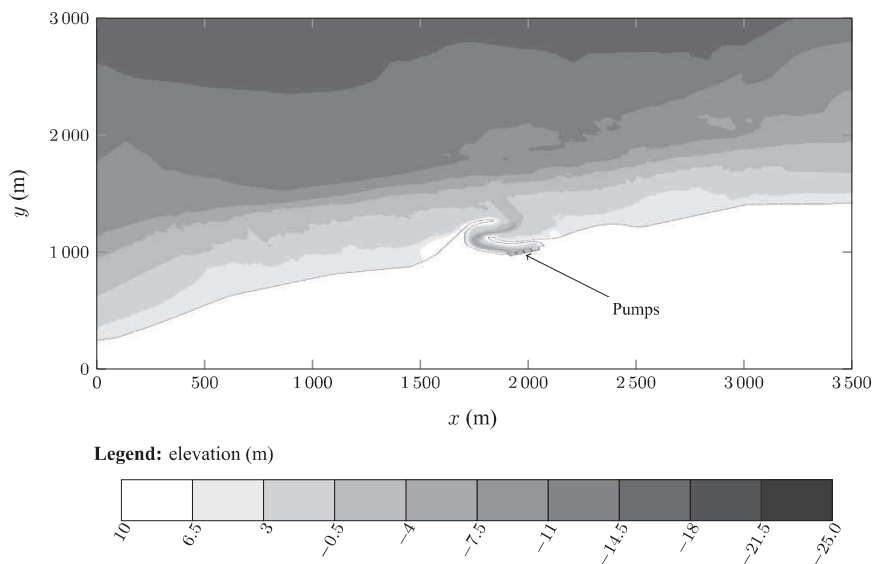


Figure 13 Example of a real bathymetry: case treated in Section 4

4 Application to environmental studies

Now that the validity of using a hybrid Eulerian–Lagrangian approach to model the transport of particles in inhomogeneous flows has been shown, the evolution of a group of particles along a realistic bathymetry surrounding a schematic harbour pumping sea water will be tested. The bathymetry and position of the pumps are shown in Fig. 13.

The flow around this structure is solved using Telemac-2D, where the effect of waves on the current is taken into account in order to create a recirculation zone west of the pump channel, see, Issa *et al.* (2009), for more details. Particles, defined by $R \approx$

4000 , $S \approx 1 - 30$, $\rho_s/\rho_f = 1.05$ and $G_p = 0.2 - 4$, are released just before the high tide and their transport is calculated using Eqs. (8a)–(8c). The influence of the different force components was tested, and it has been found that it is necessary to include all of the components described in Eq. (5), as each addition modifies the transport pattern (July 2011).

Figure 14 shows the evolution of a group of particles during one tide cycle. From this figure, it is seen that introducing a recirculation pattern in the flow traps the particles until the tide reverses. Then, particles follow the tidal current and go through the harbour channel to enter the pumps. Furthermore, Fig. 14 shows qualitatively that the particle transport model presented in

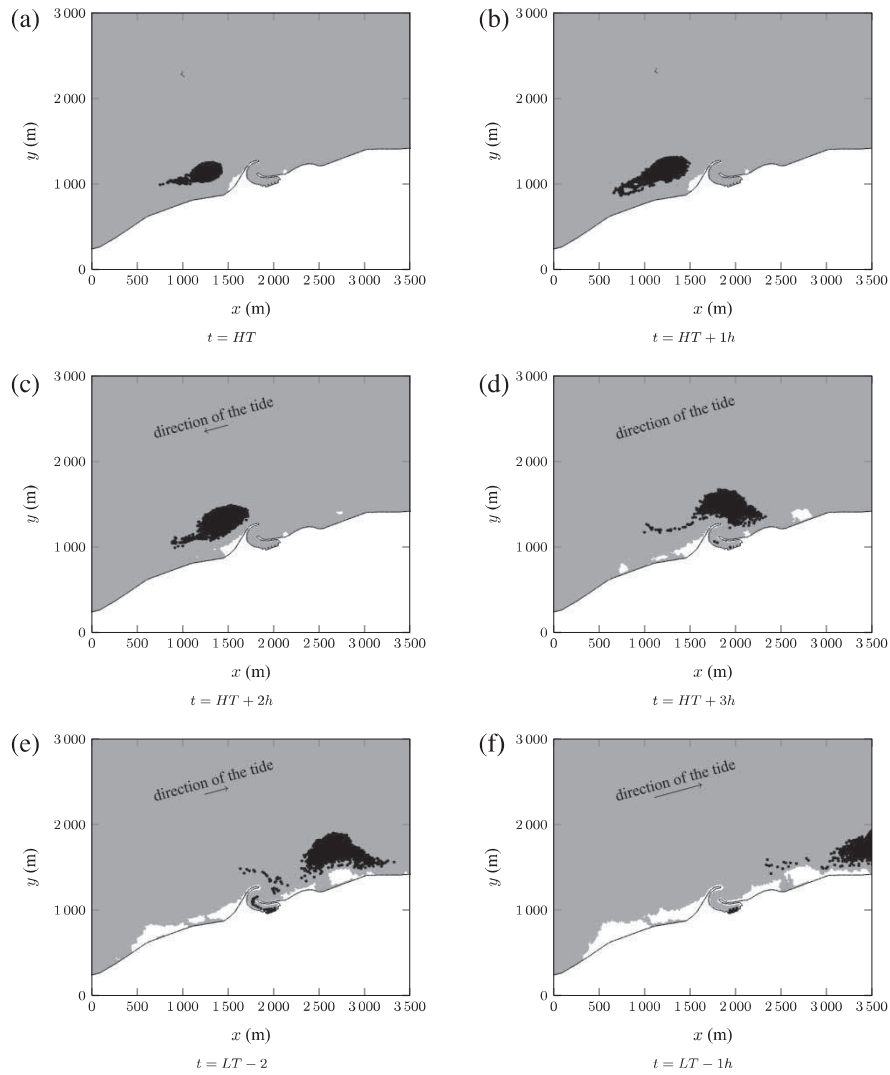


Figure 14 Modelling the real case of Fig. 13: evolution during one tide cycle of particles released just before high tide. “HT” stands for high tide and “LT” stands for low tide

this paper can model the transport in a complex flow geometry, and can help in a decisional process. A detailed description of the influence of each modelled force component on the transport of solid particles, as well as extensions of this particle transport model to algae transport can be found in Joly (2011). Furthermore, in Joly (2011), the particle transport model presented in this paper is also compared with Brownian motion.

5 Conclusions

In this paper, a Lagrangian stochastic particle transport model is developed, in view of proposing a method to predict the transport of rather large inertial particles in a coastal environment. This model is then compared with measurements of spherical particles released in a partially obstructed channel. This test is done using two different Eulerian mean flow solvers, Telemac-2D and OpenFoam, with satisfactory agreement with the experimental results. It is later tested in a realistic flow using

Telemac-2D. The Lagrangian stochastic particle transport model presented in this paper can, therefore, be easily used to calculate the transport of large groups of particles in complex flows.

In the case of the partially obstructed channel, even if OpenFoam gives better prediction of the fluid velocities, Telemac-2D is able to predict the diffusion of the particles more accurately. This is probably because the values for k are better predicted with Telemac-2D around the dike. In addition to this, for the type of particles chosen in the experiment, implementing the inertial components of the particles gives only a slight improvement in predicting the trapping of particles by the recirculation zone. It is nonetheless recommended to use a full description of the particle transport when modelling real simulations, as minute difference can greatly modify the trajectories after a large displacement. Furthermore, including all these forces allows this model to be adapted to real particles found in environmental coastal flows, such as algae, where modified added mass tensor and drag coefficients need to be used. Joly (2011) shows an application of the model to an *Ulva* algae bloom.

Notation

C_D	= drag coefficient
G_p	= gravity parameter
M_{ij}	= added mass tensor
P	= fluid pressure
S	= cross-sectional area of a particle
U_i	= fluid velocity
V_i	= particle velocity
Ω	= volume of a particle
ρ_f	= density of the fluid
ρ_s	= density of a particle
ρ_s/ρ_f	= density ratio
S	= stokes number
ε	= turbulent energy dissipation rate
k	= turbulent kinetic energy
m	= mass of a particle
R	= particle Reynolds number

References

- Almedeij, J. (2008). Drag coefficient of flow around a sphere: Matching asymptotically the wide trend. *Powder Technol.* 186, 218–223.
- Bialik, R.J. (2011). Particle–particle collision in Lagrangian modelling of saltating grains. *J. Hydraulic Res.* 49(1), 23–31.
- Chanson, H. (2008). Acoustic Doppler velocimetry (ADV) in the field and in laboratory: practical experiences. Proc. *International meeting on measurements and hydraulics of sewers*, F. Larrarte and H. Chanson, eds. Brisbane, Australia.
- Corrsin, S., Lumley, J. (1956). On the equation of motion for a particle in turbulent fluid. *Appl. Sci. Res.* 6(2–3), 114–116.
- Csanady, G.T. (1963). Turbulent diffusion of heavy particles in the atmosphere. *J. Atmospheric Sci.* 20, 201–208.
- Domgin, J., Huilier, D., Burnage, H., Gardin, P. (1997). Coupling of a Lagrangian model with a CFD code: Application to the numerical modelling of the turbulent dispersion of droplets in a turbulent pipe flow. *J. Hydraulic Res.* 35(4), 473–490.
- Donaghay, P., Osborn, T. (1997). Toward a theory of biological–physical control of harmful algal bloom dynamics and impacts. *Am. Soc. Limnol. Oceanogr.* 42, 1283–1296.
- Ettema, R., Muste, M. (2002). Scale-effect trends in hydraulic models of flow at a dike in a flat-bed channel. Technical report, Hydroscience & Engineering.
- Falkovich, G. (2011). *Fluid mechanics (A short course for physicists)*. Cambridge University Press, Cambridge.
- Frey, P., Champagne, J.-Y., Morel, R., Gay, B. (1993). Hydrodynamics fields and solid particles transport in a settling tank. *J. Hydraulic Res.* 31(6), 763–776.
- Gaylord, B., Blanchette, C., Denny, M. (1994). Mechanical consequences of size in wave-swept algae. *Ecol. Monogr.* 64(3), 287–313.
- Heemink, A.W. (1990). Stochastic modelling of dispersion in shallow water. *Stoch. Hydrol. Hydraulics* 4, 161–174.
- Hervouet, J.-M. (2007). *Hydrodynamics of free surface flows*. Wiley, Chichester.
- van Hinsberg, M.A.T., ten Thije Boonkkamp, J.H.M., Clercx, H.J.H. (2011). An efficient, second order method for the approximation of the Basset history force. *J. Comput. Phys.* 230, 1465–1478.
- Issa, R., Rougé, D., Benoit, M., Violeau, D., Joly, A. (2009). Modelling algae transport in coastal area with the shallow water equations. *J. Hydro-Environ. Res.* 3, 215–223.
- Joly, A. (2011). Modelling of the transport of algae in a coastal environment using a stochastic method. *PhD thesis*. Université Paris-Est.
- Joly, A., Moulin, F., Cazin, S., Astruc, A., Violeau, D. (2011). Experimental measurements of macro-particle dispersion in grid turbulence and application to a stochastic numerical model for solid body turbulent diffusion. Proc. *Computational Methods in Multiphase Flow VI*, 107–116. Kos, Greece.
- Joly, A., Violeau, D., Minier, J. (2010). Modelling of the turbulent diffusion of algae in a coastal environment through a stochastic method with an exact integrator. Proc. *1st European IAHR congress*, Edinburgh, Scotland.
- Landau, L., Lifchitz, E. (1987). *A course in theoretical physics: Fluid mechanics*. Pergamon Press Ltd., Oxford.
- Launder, B.E., Sharma, B.I. (1974). Application of the energy-dissipation model of turbulence to the calculation of flow near a spinning disc. *Lett. Heat Mass Transfer* 1, 131–137.
- Maxey, M.R., Riley, J.J. (1994). Preferential concentration of particles by turbulence. *Int. J. Multiphase Flow* 20(Suppl.), 169–209.
- Minier, J.-P., Peirano, E. (2001). The pdf approach to turbulent polydispersed two-phase flows. *Phys. Reports* 352, 1–214.
- Monti, P., Leuzzi, G. (2010). Lagrangian models of dispersion in marine environment. *Environ. Fluid Mech.* 10(6), 637–656.
- Open CFD (2011). OpenFOAM user guide. <http://www.openfoam.com/>.
- Pope, S. (1994). On the relationship between stochastic Lagrangian models of turbulence and second-moment closures. *Phys. Fluids* 6(2), 973–985.
- Pope, S. (2000). *Turbulent flows*. Cambridge University Press, Cambridge.
- Salomonsen, J., Flindt, M., Geertz-Hansen, O., Johansen, C. (1999). Modelling advective transport of *Ulva lactuca* (L) in the sheltered bay, Møllekrogen, Roskilde Fjord, Denmark. *Hydrobiologia* 397, 241–252.
- Sawford, B.L., Guest, F.M. (1991). Lagrangian statistical simulation of the turbulent motion of heavy particles. *Boundary-Layer Meteorol.* 54(1–2), 147–166.
- Stijnen, J.W., Heemink, H.W., Lin, H.X. (2006). An efficient 3D particle transport model for use in stratified flow. *Int. J. Numer. Methods Fluids* 56, 331–350.
- Tang, X., Ding, X., Chen, Z. (2006). Large eddy simulations of three-dimensional flows around a spur dike. *Tsinghua Sci. Technol.* 11(1), 117–123.

- Uhlmann, M. (2008). Interface-resolved direct numerical simulation of vertical particulate channel flow in the turbulent regime. *Phys. Fluids* 20(5), 053305.
- Uijttewaal, W. (2005). Effects of groyne layout on the flow in groyne fields: Laboratory experiments. *J. Hydraulic Eng.* 131(9), 782–791.
- Yeganeh-Bakhtiary, A., Shabani, B., Gotoh, H., Wang, S.S. (2009). A three-dimensional distinct element model for bed-load transport. *J. Hydraulic Res.* 47(2), 203–212.
- Yeo, K., Dong, S., Climent, E., Maxey, M.R. (2010). Modulation of homogeneous turbulence seeded with finite size bubbles or particles. *Int. J. Multiphase Flow* 36, 221–233.